Proceedings World Geothermal Congress 2020+1
Reykjavik, Iceland, April - October 2021

Insights into the Physical-Chemical Properties of a CO_2-Responsive Fracturing Fluid

Leonard F. Pease,[1] Andrew P. Kuprat,[2] Gao Dai,[1] Alain Bonneville,[1] Mark D. White,[1] Carlos A. Fernandez[1*]

[1]Energy and Environment Directorate, Pacific Northwest National Laboratory, Richland Washington.

[2]Earth and Biological Sciences Directorate, Pacific Northwest National Laboratory, Richland Washington.

* Corresponding author: Carlos.Fernandez@pnnl.gov

Keywords: fracturing fluid, polyallylamine, carbon dioxide, density, equation of state, phase diagram

ABSTRACT

Here we determine the phase behavior of StimuFrac, a CO_2 responsive fracturing fluid, under geothermal wellbore conditions. StimuFrac is an aqueous poly(allylamine) fluid that crosslinks in the presence of CO_2. StimuFrac significantly reduces the net pressure required to induce fractures, relative to other fracture fluids, and has potential to reduce water use. However, the phase behavior and equations of state to describe StimuFrac's phase behavior remain unavailable. Here we determine the density and molar volume of the fluid as a function of geothermal relevant temperatures, pressures, and weight fractions of StimuFrac added. In general, experiments find that StimuFrac's density decreases as temperature and pressure increase along the phase envelope. Using these results, equations of saturated state and phase diagrams for different polymer concentrations are reported. These results are critical inputs for planned numerical simulation efforts.

1. INTRODUCTION

Currently, stimulation methods for enhanced geothermal systems (EGS) use very large volumes of water (500,000 – 2,000,000 bbl) to create and propagate fractures and enhance reservoir permeability. Methods typically used in oil and gas development are not appropriate for EGS. For example, Slickwater polymer systems, crosslinked synthetic polymers, and surfactants are not stable at higher temperatures (150-400°C) and can cause irreversible formation damage (Waxman, et al., 2011; Tollefson, 2013; Dunham, 2012; Burden, et al., 2015).

StimuFrac is a stimulation fluid technology that consists of an aqueous polymer solution that undergoes CO_2-promoted volumetric expansions triggered by temperature. StimuFrac is distinct from conventional polymer systems used in hydraulic fracturing operations, because it is the only technology with (a) uniquely controlled CO_2-triggered volume expansion (Jung, et al., 2015), (b) reversible rheology (Jung, et al., 2015), (c) reduced water requirements (Dunham, 2012; Burden, et al., 2015; Jung, et al., 2015; Shao, et al., 2015, 2018), (d) negligible toxicity, (e) high thermal stability (up to 400°C) (Dunham, 2012; Burden, et al., 2015; Jung, et al., 2015; Shao, et al., 2015, 2018), and (f) reversible volume expansion. At the lab-scale (cubic-inch rock samples), the stress associated with this expansion in volume has been shown to consistently create fracture networks through highly impermeable rock under EGS conditions. The significantly lower effective pressure measured when applying StimuFrac compared to the pressures required for alternative fracturing fluids (water, CO_2, and their combination), together with the notable enhancement in permeability, suggests the potential of StimuFrac for cost-effective geothermal energy production with reduced impact to the environment. Despite StimuFrac's potential, key questions remain that can only be answered with quantitative evaluation of physical StimuFrac's physical properties.

Therefore, the objective of this paper is to determine the phase diagrams at representative reservoir temperatures (100-200°C) and pressures (up to 5650 psi or 39.0 MPa) with equations of state for the phase boundaries to permit numerical interpolation. In the remainder of this manuscript, the experimental system and data collected are first described. Then the equation-of-state approach is presented. Finally, the phase diagrams are presented along with experimental data versus temperature, pressure, and added polymer weight fraction. These results are essential to designing and evaluating deployment strategies with numerical modeling.

2. METHODS

2.1 Experimental Determination of Density and Molar Volume

To numerically determine StimuFrac's phase states at a range of geothermally relevant conditions, a battery of experimental measurements was performed across a range of pressures, temperatures, and added polymer concentrations. The StimuFrac fluid used in this work was prepared by diluting with water a 20 wt% aqueous solution of poly(allylamine) (PAA) (weight average MW ~17 000 g/mol; Sigma Aldrich) to obtain 0.5, 1.0, and 2.0 wt% solutions of PAA. The solution consisted of only PAA polymer and distilled deionized water without any additives. Prior to addition, the PAA had not been reacted to induce crosslinking and remained in its neutral form in all cases.

Experiments were performed in a high pressure/high temperature transmission view cell with an internal volume of 11.2 mL (excluding stirrer and in-cell pressure transducer) and sapphire windows. The view cell was insulated with foam and heated using heating cartridges driven by a PID temperature controller based on a type J thermocouple immersed within the PAA aqueous solution. A glass syringe was used to add the polymer solution to the view cell. Carbon dioxide was introduced to the view cell using an ISCO 100DX pump through a thermally insulated line (inner diameter = 1.08 mm) heated to the same temperature as the transmission vessel. The temperature in the pump itself was measured with a type J thermocouple connected at the end of the pump head and determined to be substantially equivalent to the laboratory room temperature. The line delivering CO_2 was heated

with heating tape and insulated with foam. The temperature of the CO_2 delivery line was controlled with a second PID temperature controller and maintained to the same temperature as the view cell.

In a typical experiment, 5 mL of (0.5, 1.0, or 2.0 wt%) aqueous PAA were injected into the empty view cell and heated up to the target temperature (100, 135, 170, or 200°C) while stirring. Stirring of the fluid was performed at the same speed for all the experiments. Once the temperature was constant (±1°C), CO_2 was injected first at constant pressure (8.3 MPa or 1200 psi) by opening the valve to the vessel until flow fell below 0.01 mL/min. Then, the pump was switched to constant flow and run at 0.05 mL/min as provided by the pump controller. Experiments were continuously stepped through selected pressures until the pressure in the pump achieved 39.0 MPa (5650 psi). Cell pressures were increased by pumping in CO_2 over the course of each 2-3 hour experiment. Parameters including pump pressure, CO_2 volume, flow rates, and view cell pressure and temperature were all monitored and logged using LabView Professional Development System 2016 version 16.0. Video recording of fluid behavior was performed by means of a high definition Celestron Handheld Digital Microscope PRO 5MP camera.

Video movie files of each experiment were viewed and stopped at times in the movie corresponding to cell pressures between 8.3 MPa (1200 psi) and 39.0 MPa (5650 psi) at multiples of (3.4 MPa) 500 psi (e.g., (10.3 MPa) 1500 psi, (13.8 MPa) 2000 psi, etc.). Over the temperature and pressure range explored, the fluid remained in two phases separated by a distinct meniscus: an upper CO_2-rich "gas" phase and a lower H_2O-rich "aqueous" phase. Between the two, there sometimes appeared a brown sheet-like region that was assumed to be PAA-rich. However, the appearance of brown layer with the other two phases did not follow a clear pattern. For example, this brown layer appeared within the view window in all the 100°C and 170°C runs and in all of the 200°C runs except at 1.0 wt% PAA run. It did not appear in any of the 135°C runs. Therefore, this sheet-like phase was measured as part of the aqueous phase. In reference experiments that did not employ PAA, the brown layer did not appear. At each point where the movie was stopped, a video measurement tool (markus-bader.de/MB-Ruler) was used to determine the distance in pixels that the meniscus of the aqueous region was above the bottom of the view window. This distance was then divided by the total pixel diameter of the view window to determine a fraction $0 \leq f \leq 1$ of meniscus height compared to total view window height. This fraction f was compared to a linear calibration curve of aqueous volume versus f to determine the volume of aqueous region in the cell. The remainder of the volume of the pressure cell was attributed to the CO_2-rich 'gaseous' or vapor region of the cell.

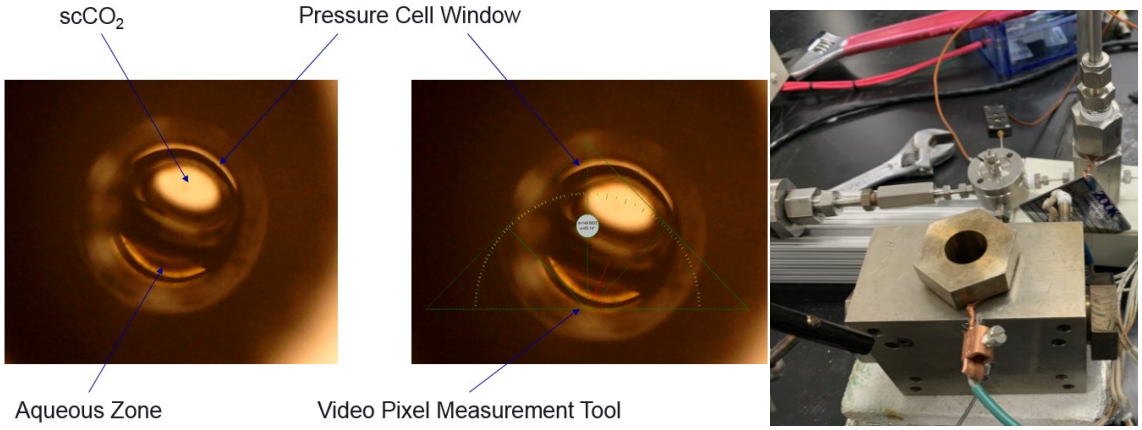

Figure 1: (left) Digital images of the view through the sapphire window of the pressure cell. (right) View of the pressure cell in the foreground with pressure cell window on top and pressurizing cylinder in the background both without superficial insulation and heating systems.

Determination of the density of the aqueous region containing PAA along with CO_2 from the vapor phase was performed as follows. A measured volume of CO_2 was driven slowly from the pump into the pressure cell, and the volume of CO_2 remaining in the pump was monitored at each pressure step. The mass of CO_2 delivered to the pressure cell was computed as being the difference between mass originally in the pump [as determined by initial volume, pressure, and temperature using the NIST webbook (webbook.nist.gov)] less remaining mass in the pump (as determined by volume and pressure in the pump at the current time) and less a small leakage mass determined as described below. The temperature of the pump was constant (~28°C) during the experiment. The pressure cell remained at the target temperature before the introduction of CO_2 heated at the same temperature measured inside the cell to permit the assumption that the gaseous portion of the cell was completely saturated with water vapor at the time of CO_2 introduction. The partial pressure of CO_2 in the gaseous region in the cell was assumed to be equal to the measured cell pressure less the known water pressure at saturation. Analysis assumed that the water vapor pressure and density both at saturation as given by NIST webbook. Also using the NIST webbook, the mass of CO_2 in the vapor portion of the cell was determined using the known temperature and partial pressure of CO_2. The difference between the total CO_2 mass delivered to the cell and the mass of CO_2 in the gaseous region was assumed to be the CO_2 mass absorbed by the aqueous region, consisting of PAA, water and CO_2. The total mass of the aqueous region was then taken to be the known initial mass of PAA and H_2O placed in cell at the beginning of the experiment less the mass of H_2O assumed to be evaporated into gaseous region plus the mass of CO_2 absorbed by the aqueous region.

To correct for any pressure cell leakage occurring over the course of the hours long experiment at high pressures, a reference experiment was performed without PAA, i.e., using only water initially in the cell with CO_2 injected at the same rate and over the same time period as the experiments with PAA. In this well characterized system, the mass of the aqueous region was calculated by assuming saturation of H_2O in the vapor region and saturation of CO_2 in the aqueous region. Specifically, by measuring aqueous volumes as above and using insight from Efika, et al., (2016) who provide the densities of the CO_2-saturated aqueous phase, predictions of aqueous masses in the reference experiment were made. These were compared to the aqueous masses determined

using the procedure described in the above paragraph. The difference between these two masses determined the leakage over the course of the reference experiment. These mass losses were added to the aqueous masses determined from the experiments with PAA.

Though the initial amount of PAA was known and recorded, the distribution of PAA polymer chain lengths was not measured so that the actual polymer composition (as opposed to the initial composition) was not determined in this analysis, even though a chemical crosslinking reaction of the PAA with CO_2 has been identified and reported. To permit use of traditional thermodynamic forms, density data were converted into a saturated liquid molar volume and a saturated vapor molar volume, assuming that the PAA completely reacted into a single polymeric molecule for all temperatures and pressures explored.

2.2 Fitting Approach

Although the videos suggest observation of three phases: a CO_2 rich vapor phase, a water rich liquid phase, and a liquid or solid PAA rich phase, numerical data obtained informed only the first two phases with the latter included in the aqueous phase. These two-phase data were fit with a cubic equation of state. Cubic equations of state were preferential for numerical simulation of StimuFrac performance due to their ability to capture intricate behavior without unnecessary mathematical complication.

As described by Smith, et al., (1996), a generalized cubic equation of state may be written as

$$P = \frac{RT}{V-b} - \frac{\theta\left(V-\eta\right)}{\left(V-b\right)\left(V^2+\delta V+\varepsilon\right)}\ , \tag{1}$$

where P is the pressure, V is the molar volume, T is the absolute temperature, R is the ideal gas constant, b represents the additional molar volume from the finite molecular size as postulated by van der Waals, and θ, η, δ, and ε are generalized constants that may be functions of temperature and pressure. The first term is an ideal gas term adjusted for this finite molecular size, and the second term represents the interparticle forces between molecules. Though both terms are important for both phases, the second term dominates the liquid behavior.

The data described above provide two points for every unique pressure-temperature-initial mass percent combination: one for the saturated liquid and one for the saturated vapor. This contrasts with the generalized cubic equation of state that requires information to determine five constants. Progress may be achieved by grouping the data for a given temperature together and fitting the saturated pressure and molar volumes across a given temperature. Put succinctly, the approach here differs from Eq. 1 in that

$$P_{sat} = \frac{RT}{V_{sat}-b} - \frac{\theta\left(V_{sat}-\eta\right)}{\left(V_{sat}-b\right)\left({V_{sat}}^2+\delta V_{sat}+\varepsilon\right)}\ , \tag{2}$$

where the subscript sat indicates evaluation at saturation but the temperature has not been marked as being saturated. This is a fundamental distinction because the resulting equations of state are predictive of physicochemical properties only at saturated conditions.

Because the first term is essentially the ideal gas law, the focus of fitting moves to the second term. To determine the fitting of the second term, Eq. 2 may be rearranged as

$$f\left(V_{sat}\right) \equiv \frac{1}{RT-P_{sat}\left(V_{sat}-b\right)} = \frac{\left({V_{sat}}^2+\delta V_{sat}+\varepsilon\right)}{\theta\left(V_{sat}-\eta\right)}. \tag{3}$$

For ease of fitting and because $V_{sat}>>b$,[1] we may approximate

$$f\left(V_{sat}\right) \equiv \frac{1}{RT-P_{sat}V_{sat}} = \frac{\left({V_{sat}}^2+\delta V_{sat}+\varepsilon\right)}{\theta\left(V_{sat}-\eta\right)}\ . \tag{4}$$

Therefore, plots of $f(V_{sat})$ versus V_{sat} may provide insight into the intermolecular interactions (for an ideal gas, $f(V_{sat})=\infty$), and one may anticipate a quadratic appearance except near a pole (i.e., where f becomes locally infinite) located at $V_{sat}=\eta$. The resulting curves may be scaled so that all of the data fall onto a single master curve and then be fit with a bipartite form as the resulting curves suggest.

Fitting of the gas phase data was accomplished in Excel, whereas the liquid phase data was fit using Mathematica, both using expressions suggested by Eq. 4. Constants determined from Eq. 4 as functions of temperature and initial polymer composition

[1] In principle, the value of b may be determined from any one of a number of different expressions, but this value is often considered to be small (Rowley, 2019). For water and CO_2 using the van der Waals and Redlich-Kwong formulations, b=2.1·10^{-5} -4.3·10^{-5} m^3/mol, which confirms that it is usually small compared to the vapor molar volumes, justifying its absence for vapor. For the liquid phase, molar volumes overlap the expected value of b. Because *V must* exceed b and because b makes little if any numerical improvement in the quality of the curve fitting, b is not included for the liquid either.

were used in Eq. 2 with b=0. Data for which the liquid density substantially exceeded that of pure liquid water were considered to be outliers.

3. RESULTS AND DISCUSSION

The objective of this study is to quantify the phase behavior of StimuFrac, a polymeric fluid, in the range of 100-200°C (212-392°F) for pressures up to 39 MPa (5650 psi) and initial PAA weight fractions of 0.5-2.0 wt%. The remainder of this paper evaluates the data obtained experimentally in the context of the fitting process described above, summarizes the resulting equations of saturated state and culminating phase diagrams, and finally presents liquid density as a function of pressure. Molar volumes and mass densities are mixture values.

3.1 Equations of Saturated State

The expression of Eq. 4 is plotted in Fig. 2 for each of the four temperatures. If the fluid were an ideal gas, the ordinate would be infinite. Yet, the data are finite at multiple conditions in the figure, indicative of significant interparticle forces relative to an ideal gas. In this form of $f(V_{sat})$ versus V_{sat}, the data do indeed collapse across initial compositions onto a single curve for each temperature. This is surprising because the composition may have been expected to play a more prominent role. Yet, the composition appears to play at most a very modest role, perhaps because the concentrations themselves are relatively modest. As suggested by Eq. 4, the saturated vapor data at larger saturated molar volumes do indeed suggest a quadratic appearance with a pole. However, the saturated liquid data are inconsistent with a quadratic-pole mathematical form. Therefore, the saturated liquid and saturated vapor are fit separately. The need to fit liquid and vapor data separately is not particularly surprising, because cubic equations of state are known to struggle with liquid-phase data.

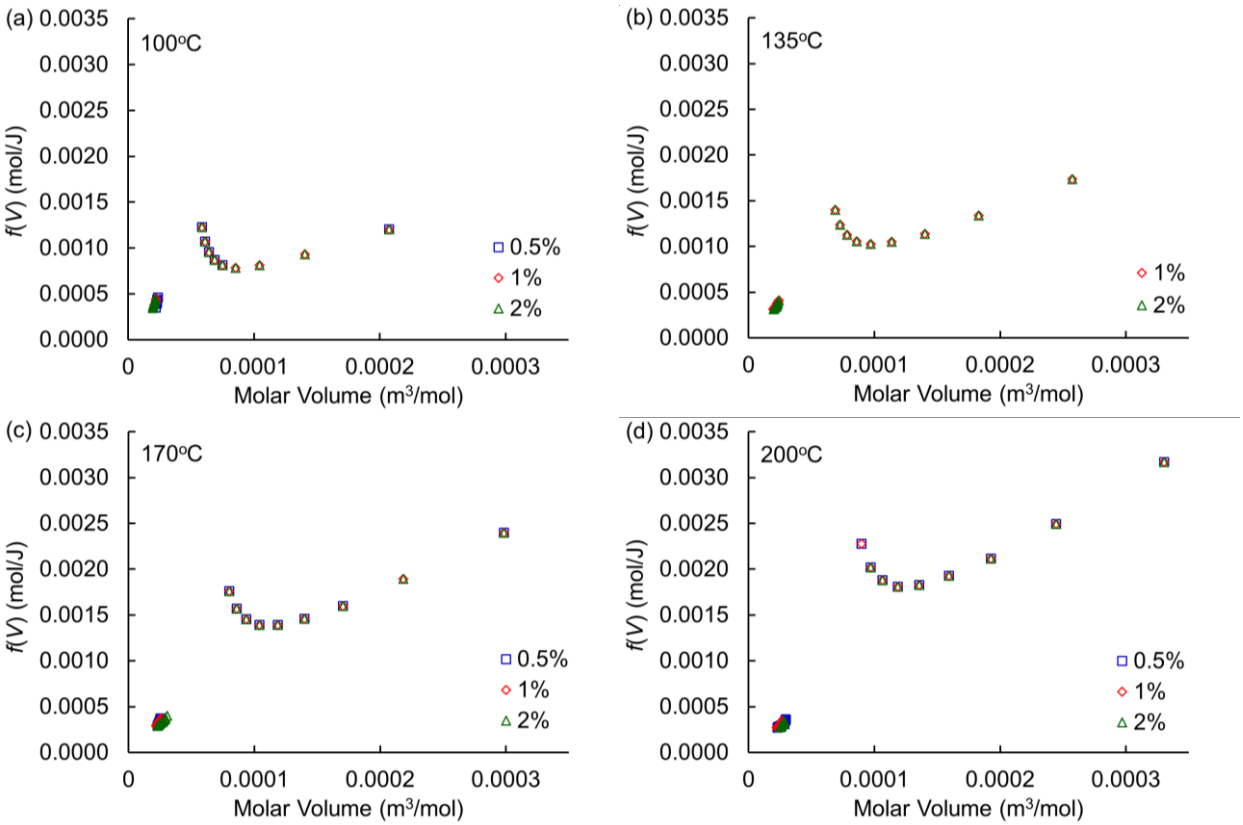

Figure 2: The expression of $f(V_{sat})$ versus V_{sat} as given in Eq. 4. The data for each temperature collapse to a single curve, and the curves across temperatures are qualitatively similar.

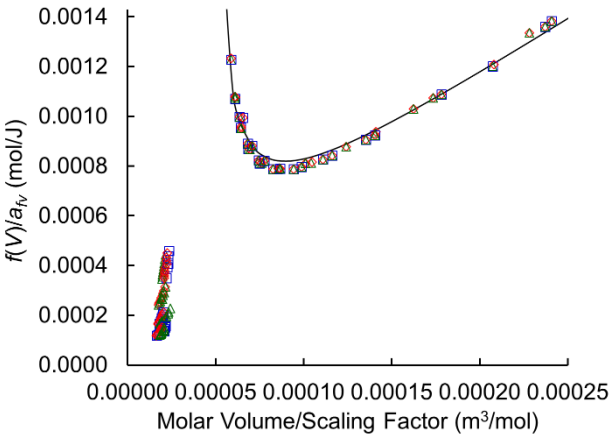

Figure 3: The expression of $f(V_{sat})$ as defined in Eq. 4 scaled on a_{fv} versus V_{sat} scaled on a_v for all of the data in Fig. 2 with corresponding symbols. Scaling factors are $a_{fv}=f(V_{sat},T)/f(V_{sat},100^oC)=(0.0000658\ K^{-2})T^2-(0.0427455\ K^{-1})T+7.7835012$ for $T>325$ K and $a_v=V_{sat}(T)/V_{sat}(100^oC)=(0.00375\ K^{-1})T-0.40271$, for both of which R^2 exceeds 0.97. Fit given as $f(V_{sat})/a_{fv}=\alpha_1(V_{sat}/a_v)^2/(V_{sat}/a_v-\alpha_2)$, where $\alpha_1=4.575\ mol^2/(J\cdot m^3)$ and $\alpha_2=0.0000448\ m^3/mol$.

Given the similarity of the curves in Fig. 2, the vapor portion of the data (larger molar volumes) may be rescaled using the minimum as a fixed point. Figure 3 shows that the vapor portions of curves at the four temperatures do indeed collapse onto a single curve with appropriate selection of temperature dependent scaling factors. The collapse of the saturated liquid data is not as compelling, indicating that saturated liquid data need separate scaling, again suggesting a bipartite result. For the vapor, we find

$$f\left(V_{sat}^{\ vap}\right)=\frac{a_{fv}\alpha_1}{a_v}\frac{\left(V_{sat}^{\ vap}\right)^2}{\left(V_{sat}^{\ vap}-a_v\alpha_2\right)}, \tag{5}$$

where a_{fv} is the scale factor for f, a_v is the scale factor for the molar volume, and α_1 and α_2 are fitting constants as determined from Fig. 3. Comparison with Eq. 4 returns $\delta=0$, $\varepsilon=0$, $\theta=a_v/(a_{fv}\alpha_1)$, and $\eta=\alpha_2 a_v$. From here, then, the equation of saturated state for the vapor becomes

$$P_{sat}=\frac{RT}{V_{sat}^{\ vap}}-\frac{\theta\left(V_{sat}^{\ vap}-\eta\right)}{\left(V_{sat}^{\ vap}\right)^3}, \tag{6}$$

where

$$\theta=\frac{\frac{0.00375}{\mathrm{K}}T-0.40271}{4.575\left(\frac{0.0000658}{\mathrm{K}^2}T^2-\frac{0.0427455}{\mathrm{K}}T+7.7835012\right)}\frac{\mathrm{J\cdot m^3}}{\mathrm{mol^2}} \tag{7}$$

and

$$\eta=0.0000448\left(\frac{0.00375}{\mathrm{K}}T-0.40271\right)\frac{\mathrm{m^3}}{\mathrm{mol}}, \tag{8}$$

where the temperatures here are absolute temperatures (K), and w is in mass percent not mass fraction. This expression is compared to data in Fig. 4.

Separately, the saturated liquid data, $f(V_{sat}^{liq})$ versus V_{sat}^{liq}, may be fit across all of the data with a polynomial in V_{sat}^{liq} that has coefficients β_i that depend on temperature T and mass percent w. The selected quadratic polynomial,

$$f\left(V_{sat}^{\ liq}\right)=\beta_o+\beta_1 V_{sat}^{\ liq}+\beta_2\left(V_{sat}^{\ liq}\right)^2, \tag{9}$$

is chosen in the spirit of a cubic equation of state. After fitting, the coefficients, β_i, become

$$\beta_o=\left(\begin{array}{l}-0.028317+\frac{0.00014729}{\mathrm{K}}T-\frac{2.1779\times10^{-7}}{\mathrm{K}^2}T^2+\frac{7.7492\times10^{-11}}{\mathrm{K}^3}T^3\\+0.0018059w-\frac{0.000012591}{\mathrm{K}}Tw+\frac{1.0244\times10^{-8}}{\mathrm{K}^2}T^2w+0.0013824w^2\\+\frac{2.5394\times10^{-7}}{\mathrm{K}}Tw^2-0.00040416w^3\end{array}\right)\frac{\mathrm{mol}}{\mathrm{J}}, \tag{10}$$

$$\beta_1 = \left(861.17 - \frac{4.2567}{\mathrm{K}}T + \frac{0.0050647}{\mathrm{K}^2}T^2 - 26.340w + \frac{0.11578}{\mathrm{K}}Tw - 5.1227w^2\right)\frac{\mathrm{mol}^2}{\mathrm{J}\cdot\mathrm{m}^3}, \tag{11}$$

and

$$\beta_2 = \left(6.2541\times10^6 - \frac{12176}{\mathrm{K}}T - 280144w\right)\frac{\mathrm{mol}^3}{\mathrm{J}\cdot\mathrm{m}^6}, \tag{12}$$

where the temperatures here are absolute temperatures (K), and w is in mass percent not mass fraction. Then, the equation of saturated liquid state becomes

$$P_{sat} = \frac{RT}{V_{sat}^{\ liq}} - \frac{1}{\beta_o V_{sat}^{\ liq} + \beta_1 \left(V_{sat}^{\ liq}\right)^2 + \beta_2 \left(V_{sat}^{\ liq}\right)^3}. \tag{13}$$

The results of this fitting process are also shown in Fig. 4.

3.2 Phase Diagrams and Density Plots

Figure 4 presents phase diagrams predicted from Eqs. 6 and 13. In the figure, the curves at lower molar volumes represent the boundary between liquid only regions and the two-phase saturated region; curves at higher molar volumes represent the boundary between vapor only and the two-phase saturated region. For the vapor boundary, the overlap between the experimental data and equation of saturated state prediction remains remarkably close. Though not perfect, the fits are quite reasonable with essentially a single curve for each temperature. For the liquid boundary, the overlap between the experimental data and equation of saturated state prediction remains reasonable. In contrast to the vapor boundary, the saturated liquid boundary appears to depend on both temperature and on the added PAA mass.

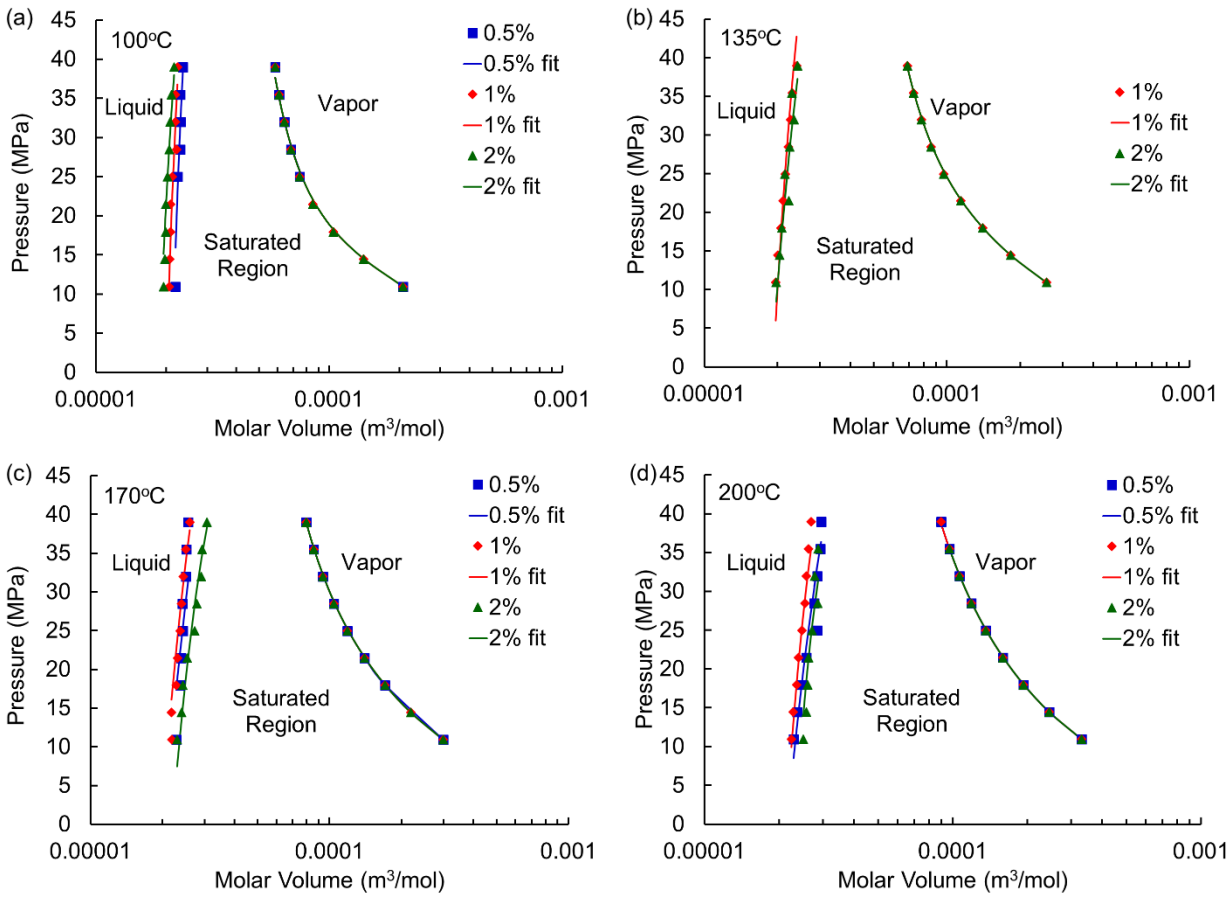

Figure 4: Phase diagrams highlighting the saturation envelope that follows from Eqs. 6 and 13.

The information in Fig. 4 may be converted into plots of density versus pressure as seen in Fig. 5. In general, the experiments found that aqueous phase density decreased as pressure increased along the phase envelop. The match between experiment and prediction remains quite reasonable given that at least some of the variation is experimental. Nevertheless, these results provide critical insight and essential inputs to numerical simulation efforts to come.

4. CONCLUSIONS

In this study, we evaluated the phase behavior of StimuFrac, a PAA rich aqueous fluid known to polymerize in the presence of CO_2. High pressure/high temperature measurements determined the phase envelope in the range of 100-200°C, at pressures at or below 39.0 MPa (5650 psi), and for PAA additions of 0.5-2.0 wt%. Equations of saturated state were used to describe the phase envelope over the range of interest, essential to generating phase diagrams. Predictions of the curves for density versus pressure at saturation across temperatures and added PAA remain in reasonable agreement with experimental determinations of the same.

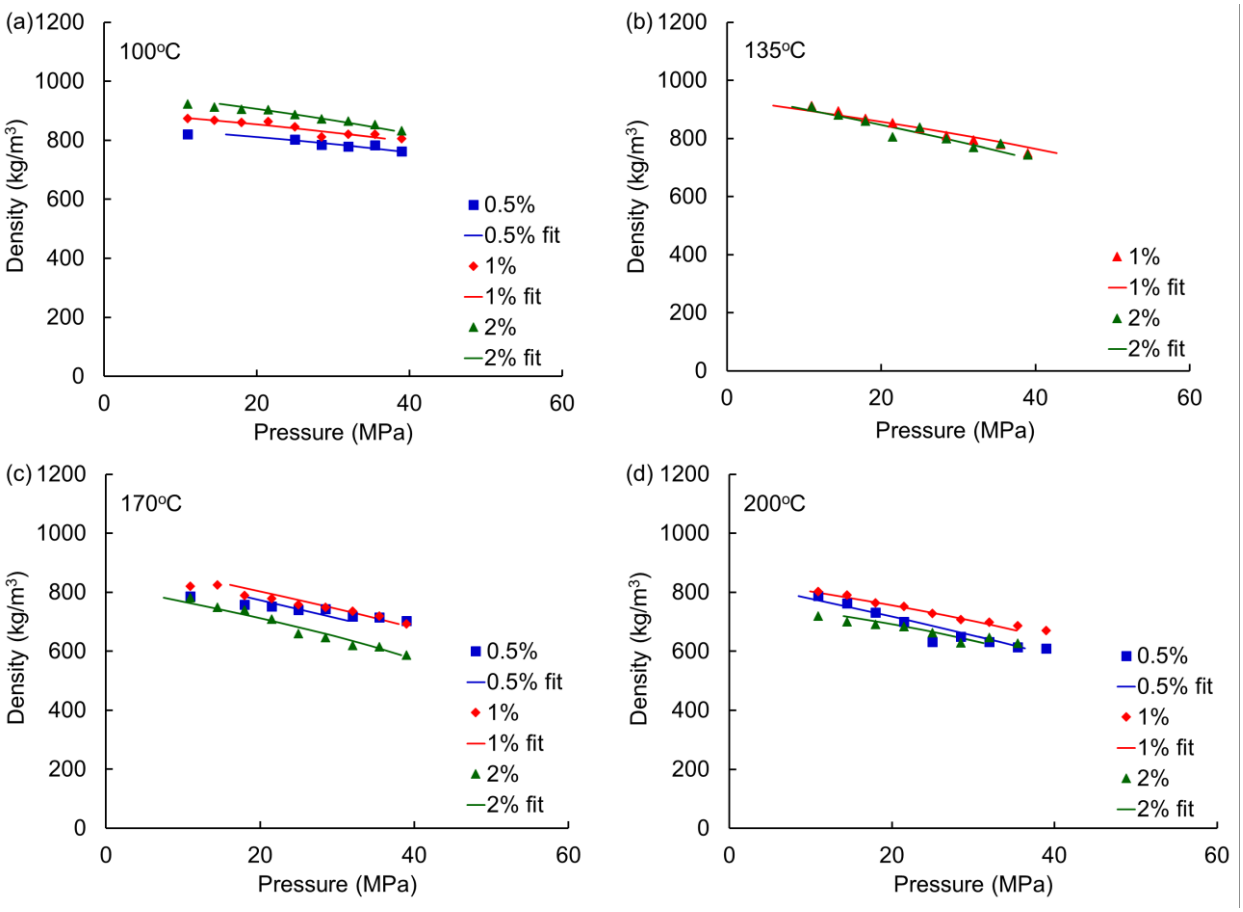

Figure 5: Liquid density versus pressure at saturation along the phase envelope. Conversions from molar volume to density used an approximate molecular weight of 18 g/mol; the average liquid molecular weight varies from 18.0-22.0 g/mol with the addition of CO_2.

5. ACKNOWLEDGEMENTS

Funding for this research was provided by the U.S. Department of Energy's Geothermal Technology Office. Pacific Northwest National Laboratory (PNNL) is a multiprogram national laboratory operated for the U.S. Department of Energy by Battelle Memorial Institute under Contract DE-AC05-76RL01830.

6. REFERENCES

Burden, S., Dean, J., Koplos, J., Meza-Cuadra, C., Singer, A., Tuccillo, M.E.: Analysis of Hydraulic Fracturing Fluid Data from the FracFocus Chemical Disclosure Registry 1.0, Office of Research and Development, U.S. Environmental Protection Agency, Washington, DC., EPA/601/R-14/003 (2015).

Dunham, J.: Business Impact of Proposed Changes to Well Completion Regulations, *Dunham and Associates*, 2012, https://www.westernenergyalliance.org/wp-content/uploads/2012/05/Revised-Cost-Memo.pdf, downloaded 7/29/2019.

Efika, E.C., Hoballah, R., Li, X., May, E.F., Nania, M., Sanchez-Vicente, Y., and Trusler, J.P.M.: Saturated Phase Densities of (CO_2 + H2O) at Temperatures from (293 to 450) K and Pressures up to 64 MPa, *J. Chem. Thermo.*, **93**, (2016), 347–359.

Jung H.B., Carroll, K.C., Kabilan, S., Heldebrant, D.J., Hoyt, D.W., Zhong, L., Varga, T., Stephens, S., Adams, L., Bonneville, A., Kuprat, A., and Fernandez, C.A.: Stimuli-Responsive/Rheoreversible Hydraulic Fracturing Fluids as a Greener Alternative to Support Geothermal and Fossil Energy Production, *Green Chemistry*, **17** (2015), 2799-2812, doi:10.1039/c4gc01917b.

Rowley, R.L.: www.et.byu.edu/~rowley/ChEn273/Topics/Mass_Balances/Single_Phase_Systems/Corresponding_States.htm, downloaded 7/29/2019.

Shao H., Kabilan, S., Stephens, S., Suresh, N., Beck, A.N., Varga, T., Martin, P.F., Kuprat, A. Jung, H.B., Um, W., Bonneville, A., Heldebrant, D.J., Carroll, K.C., Moore, J., and Fernandez, C.A.: Environmentally Friendly, Rheoreversible, Hydraulic-fracturing Fluids for Enhanced Geothermal Systems, Geothermics, **58**, (2015), 22-31, doi:10.1016/j.geothermics.2015.07.010.

Shao H., Kabilan, S., Childers, M.I., Stephens, S., Suresh, N., Beck, A.N., Varga, T., Martin, P.F., Kuprat, A. Jung, H.B., Um, W., Bonneville, A., Heldebrant, D.J., Carroll, K.C., Moore, J., and Fernandez, C.A.: Corrigendum to "Environmentally Friendly, Rheoreversible, Hydraulic Fracturing Fluids for Enhanced Geothermal Systems" [Geothermics 58 (2015) 22-31]. Geothermics, **72** (2018) 323-325, doi:10.1016/j.geothermics.2017.12.002.

Smith, J.M., Van Ness, H.C., and Abbot, M.M.: Introduction to Chemical Engineering Thermodynamics. McGraw-Hill: New York, 1996.

Tollefson, J.: Secrets of Fracking Fluids Pave Way for Cleaner Recipe, *Nature*, **501** (2013), 146-147, doi:10.1038/501146a.

Waxman, H.A., Markey, E.J., and DeGette, D.: Chemicals Used in Hydraulic Fracturing, Minority Staff of Committee on Energy and Commerce, *United States House of Representatives*, Washington D.C. (2011).